NANO LETTERS

Letter

pubs.acs.org/NanoLett

Nanoscale Mapping of the Magnetic Properties of (111)-Oriented $La_{0.67}Sr_{0.33}MnO_3$

Kerry J. O'Shea,[†] Donald A. MacLaren,*[,†] Damien McGrouther,[†] Danny Schwarzbach,[‡] Markus Jungbauer,[‡] Sebastian Hühn,[‡] Vasily Moshnyaga,[‡] and Robert L. Stamps[†]

[†]SUPA, School of Physics and Astronomy, University of Glasgow, G12 8QQ, Glasgow, United Kingdom

[‡]I. Physikalisches Institut, Georg-August-Universität Göttingen, Friedrich-Hund-Platz 1, 37077 Göttingen, Germany

Supporting Information

ABSTRACT: Spatially resolved analysis of magnetic properties on the nanoscale remains challenging, yet strain and defects on this length-scale can profoundly affect a material's bulk performance. We present a detailed investigation of the magnetic properties of $La_{0.67}Sr_{0.33}MnO_3$ thin films in both free-standing and nanowire form and assess the role of strain and local defects in modifying the films' magnetic properties. Lorentz transmission electron microscopy is used to measure the magnetocrystalline anisotropy and to map the Curie temperature and saturation magnetization with nanometric spatial resolution. Atomic-scale defects are identified as pinning sites for magnetic domain wall propagation. Measurement of domain wall widths and crystalline strain are used to identify a strong magnetoelastic contribution to the magnetic anisotropy. Together, these results provide unique insight into the relationship between the nanostructure and magnetic functionality of a ferromagnetic complex oxide film.

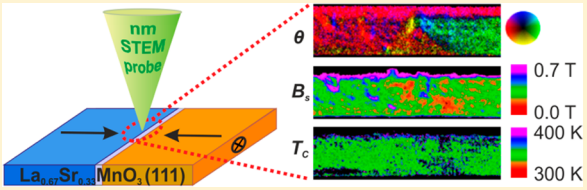

KEYWORDS: *LSMO, magnetic domain wall, Lorentz TEM, high-spatial resolution, spintronics*

The multiplicity of functionalities available in heteroepitaxial complex oxides has stimulated intense research in recent years and suggests a variety of future microelectronic technologies.[1−6] $La_{1-x}Sr_xMnO_3$ (LSMO) is one of the most studied perovskite oxides because at an optimal Sr doping of x = 0.33 it exhibits colossal magnetoresistance, high spin-polarization, and a relatively high Curie temperature of 370 K. These properties are known to be sensitive to compositional variations, particularly changes to the Sr concentration or oxygen content.[6] Epitaxial strain is also inevitable in most device configurations and can be used to manipulate[7] the LSMO magnetocrystalline anisotropy,[8] exchange bias,[9] and magnetoelectric coupling.[1] For example, a lattice mismatch with either $LaAlO_3$[10−12] or $NdGaO_3$[13−16] substrates causes a compressive strain in a deposited LSMO thin film while $SrTiO_3$ (STO) substrates lead to a tensile strain. The resulting anisotropy depends on the substrate orientation[8,17−21] and in the case of vicinal substrates can be used to induce a uniaxial magnetic anisotropy,[22−25] just as in metallic ferromagnets.[26] However, previous reports also indicate that the magnetic and electronic properties of LSMO are sensitive to structural defects such as grain boundaries[27] or the type of ion-induced damage that might arise during patterning,[28] and there has been much discussion of the origin and extent of magnetic "dead layers" at the surface of LSMO thin films.[29,30] A full understanding of the intrinsic magnetic properties of LSMO, and their dependence on defects and strain, is therefore critical for the future exploitation of LSMO in device applications. Assessment of the intrinsic properties, that is, in the absence of epitaxial strain, can be hard to achieve but here we characterize the properties of a largely strain-free, free-standing LSMO film. We consider (111)-oriented LSMO, motivated in part by the enhanced structural and electronic coupling that arises at epitaxial interfaces to produce new topological phases[31] and, interestingly, exchange bias in (111)-oriented superlattices.[32]

A variety of techniques have previously been used to image the magnetic domain structure of LSMO films and nanostructures, including Kerr microscopy,[33] magnetic force microscopy,[34−36] scanning electron microscopy,[37] and photoemission electron microscopy;[38−40] however, these techniques are either limited in terms of spatial resolution, which is typically tens of nanometers[41] or are purely surface sensitive and therefore blind to bulk structures. Conversely, Lorentz transmission electron microscopy (TEM) can image the subsurface magnetic structure of a thin film or nanostructure[42,43] in projection or by the use of cross sections. In this Letter, we use scanning transmission electron microscopy (STEM) and Lorentz DPC microscopy to correlate the structural and functional properties of ferromagnetic oxide thin films. We demonstrate the novel capability of collecting magnetic, structural, and spectroscopic information with nanometre spatial resolution in a single experiment, complementing recent advances in analytical electron microscopy and spectroscopy[44,45] with aberration corrected Lorentz DPC imaging.[46] We use these experimental advances to measure the magnetic domain wall (DW) width of

Received: May 19, 2015
Revised: July 31, 2015
Published: August 7, 2015

DOI: 10.1021/acs.nanolett.5b01953
Nano Lett. 2015, 15, 5868−5874

a (111)-oriented $La_{0.67}Sr_{0.33}MnO_3$ single crystal film and subsequently determine the magnitude of the film's magnetic anisotropy in the absence of epitaxial strain. We map variations in the Curie temperature and assess the role of defects and damage in modulating local magnetic properties on the nanoscale, including the pinning of magnetic domain walls.

EXPERIMENTAL METHODS

A 120 nm thick $La_{0.67}Sr_{0.33}MnO_3$ film was deposited onto a $SrTiO_3$(111) substrate by metalorganic aerosol deposition.[47] Characterization of the as-deposited film is outlined in Supporting Information. In comparison to surface imaging techniques, samples for STEM characterization must be electron transparent and there has previously been difficulty in fabricating plan-view specimens from epitaxial thin films. Here, an FEI Nova focused ion beam (FIB) instrument was used to mill the STO substrate and release a largely stress-free, ~ 100 μm^2 electron transparent membrane of LSMO. Details of the specimen preparation technique can be found elsewhere.[48] A cross-section specimen was also fabricated in order to map out-of-plane structural and functional details.[49] All characterization was conducted using a JEOL ARM-200cF scanning transmission electron microscope with a beam energy of 200 keV. The instrument is equipped with a Gatan Quantum 965 spectrometer that was used for electron energy loss spectroscopy (EELS) analysis. The sample temperature was controlled using a liquid nitrogen cooled Gatan HC3500 TEM stage. A CEOS (probe) aberration corrector was used for atomic-resolved STEM imaging and can be reconfigured to reduce the dominant spherical aberration coefficient, C_s, in Lorentz mode to a few microns. This results in a Lorentz STEM probe diameter, which determines the image resolution, down to ~1 nm.[46] Magnetic characterization was performed using Lorentz DPC imaging, where the deflection of the electron diffraction disk caused by a sample's magnetization is measured using a bespoke segmented detector (see Supporting Information).[50] It is worth noting that structural and spectroscopic analysis (EELS) were performed with the objective lens switched on while the magnetic characterization was performed with the objective lens switched off to leave the sample in an effectively field-free environment.

PLANAR WINDOW AND MAGNETOELASTIC ANISOTROPY

We discuss first the freestanding LSMO membrane; its analysis is summarized in Figure 1. A low-magnification (room temperature) bright-field TEM image of the membrane is given in Figure 1a. The membrane is imaged down the [111] axis and the (inset) selected area diffraction pattern indicates the long edge of the electron transparent region to be aligned approximately along a ⟨110⟩-type direction, as indicated. (Note that we use pseudocubic indexing for ease.) Image contrast is dominated by thickness fringes and a low density of bend contours that arise from electron interference effects[52] but do not hinder subsequent magnetic characterization. The diffraction pattern indicates that the membrane is single crystalline, from which we infer that any damage that occurred during specimen preparation has not impaired the membrane structure. DPC imaging (see schematic in Figure 1b,c) was used to acquire a pair of orthogonal magnetic induction maps from the region enclosed by the red box in Figure 1a and in turn these were used to generate the color map in Figure 1d,

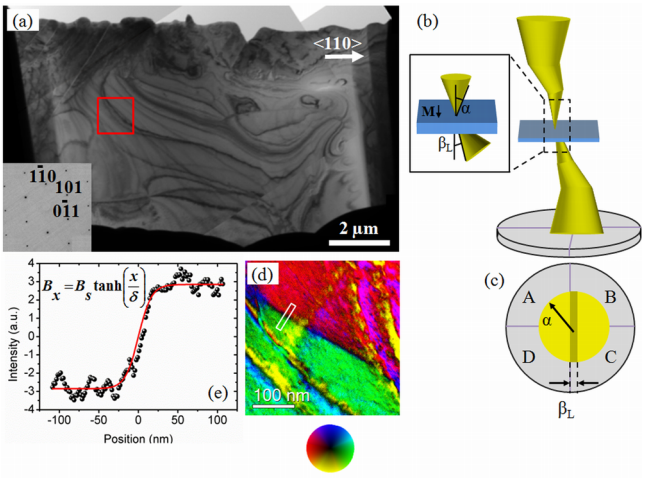

Figure 1. (a) Low-magnification TEM overview of the unsupported LSMO window with selected area diffraction pattern inset. The red box indicates the region from which the DPC images were acquired. (b) A schematic illustration of the differential phase contrast mode of Lorentz microscopy, highlighting the deflection of the electron beam through angle β_L on passing through a magnetic specimen. The subsequent shift of the diffraction disc on the detector is indicated in (c), where the probe convergence angle, α, determines the diffraction disc radius. (d) Color map of magnetic induction with color wheel to indicate the direction and magnitude. (e) Intensity profile from white boxed region in (d) across the domain wall (black) with hyperbolic tangent fit (red).[51]

which illustrates vividly the in-plane magnetic domain structure. The colors (intensities) represent the direction (magnitude) of in-plane magnetic induction in accordance with the color wheel below the image. There is strong magnetic contrast superimposed onto the diffraction contrast and bend contours described above. The abrupt diagonal red-green color change is consistent with a sharp 180° DW running diagonally across the field of view: the magnetization aligns parallel to the wall, along a ⟨110⟩-type direction of the crystal in order to minimize the magnetostatic energy of the DW, while bend contours coincidentally appear as yellow/blue streaks. This bend contour contrast can be considered an artifact; it is the result of intensity changes within the diffraction disc, rather than a deflection of the disc, and is therefore not magnetic in origin.[53] It is also noted that the color intensity is reduced at the center of the DW, which is consistent with a reduction of the in-plane magnetic induction component and thus indicates a Bloch wall structure. One might anticipate the presence of three ⟨110⟩ type easy axes for LSMO(111) as a result of the 3-fold surface symmetry, however, DWs formed repeatedly and consistently with the same orientation, indicating the presence of a uniaxial anisotropy along this direction.

We can estimate the magnitude of the anisotropy by measuring the width of the 180° DW. Figure 1e plots the signal intensity across the region of the DW enclosed by the white box in Figure 1d, fitted by a hyperbolic tangent function of the form $B_y(x) = B_S \tanh(x/\delta)$, where x is the coordinate normal to the wall, B_S is the saturation induction, and δ is the wall width parameter, usually defined in terms of a DW width of $w = 1.76\delta$.[54] The DW width was measured at 10 locations along the wall in Figure 1d, yielding an average DW width of 35.8 ± 3.2 nm, which is comparable to that previously reported for other manganites (e.g., 38 nm for a DW along [100] in $LaCaMnO_3$[55] and 39 nm in $LaPrCaMnO_3$[56]), although those

DOI: 10.1021/acs.nanolett.5b01953
Nano Lett. 2015, 15, 5868−5874

values were measured at low temperature and are therefore expected to increase at room temperature. The magnitude of the anisotropy then relates to the DW width via the relation $w = \pi(A/K)^{1/2}$ if one assumes the DW width to be determined by exchange and anisotropy contributions alone.[57] Taking A to be 1.7 pJ/m,[58] the anisotropy was found to be $K_{exp} = 1.3 \times 10^4$ J/m^3, which is comparable to that of LSMO(110) ($K_U = 1.9 \times 10^4$ J/m^3).[18] We are unaware of previous measurements of the anisotropy of LSMO/STO(111) films, although $BiFeO_3$–$CoFe_2O_4$ (BFO–CFO) grown on STO(111)[59] exhibits an in-plane anisotropy due to a triangular pillar morphology of the CFO, which resulted in a strong shape anisotropy.

Turning to the origin of the above anisotropy, we expected the magnetoelastic energy to be isotropic in LSMO(111) and for the majority of the tensile lattice strain to have relaxed within ~10 nm of a well-lattice mismatched substrate,[60,61] consistent with the as-deposited film. However, slight distortion of the lamella during specimen preparation produced an out-of-plane buckling that was measured by atomic force microscopy to be ~120 nm across the ~11.7 μm width of the window, consistent with a uniform strain of 0.02%.[48] Thus, the magnitude of the resulting magnetoelastic anisotropy can be estimated using

$$K_U = -\left(\frac{3}{2}\right) Y(\Delta\varepsilon)\lambda_S \cos^2(\xi)$$

where Young's modulus is taken as Y = 562 GPa,[62] $\Delta\varepsilon$ is the estimated in-plane strain, λ_s is the saturation magnetostriction (taken as 200 ppm[63]), and ξ is the angle between the magnetization and the stress axis, which here is around 30°. We find $K_U = -2.7 \times 10^4$ J/m^3, where the negative sign implies an in-plane easy axis. The good agreement with K_{exp} indicates that even a low level of strain creates significant magnetoelastic anisotropy; the small discrepancy is attributed to minor thickness variations across the lamella.[48]

CROSS-SECTION GEOMETRY AND DOMAIN WALL PINNING

Turning now to the cross-section geometry, we find crystallographic defects to play an important role in the behavior of magnetic DWs in LSMO. We fabricated a cross-section of the same 120 nm thick $La_{0.7}Sr_{0.3}MnO_3$ film using standard FIB protocols. Using EELS to determine the thickness (see below), the resulting LSMO has the form of a long thin strip with dimensions 120 nm × 15 μm × 35 nm (width × length × thickness). The magnetic behavior is therefore expected to be constrained by a shape anisotropy imposed by the rectangular form and to have two-dimensional characteristics, as the magnetization will lie predominantly in the plane of the thin lamella. These aspects facilitate comparisons with magnetic nanowires of the literature,[64] a term that we adopt here.

A low-magnification overview is given in Figure 2a, which indicates high quality epitaxial growth of the LSMO onto the $SrTiO_3$ substrate. Regular, unexpected rectangular defects (~25 nm × 60 nm in size) were observed across the LSMO layer but were not detected in X-ray diffraction measurements (see Supporting Information) nor observed to impede DW propagation through the plan-view lamella of Figure 1a, so are assumed to be caused by mechanical stress during preparation of the cross-section. In the current context, they are fortuitous as they allow the link between LSMO magnetization and defects to be explored. A high-angle annular dark-field (HAADF) image of the region enclosed by the red box is given in Figure 2b, which shows an isolated twinning defect. The crystal is viewed down a ⟨110⟩ axis and a (111) twinning plane lies horizontally across the middle of the image. Scanning diffraction was performed across a large field of view, allowing the defect regions to be clearly distinguished, as illustrated in Figure 2c,d: each defect is a rectangular region of LSMO that is in a twin orientation with the surrounding film. Selected area diffraction patterns from different regions of the lamella were superimposed using false-color in order to highlight different features, that is, red diffraction spots in Figure 2d derive from the defect regions, which are vividly picked out from the surrounding LSMO matrix in Figure 2c. Similarly, the green, yellow, and blue features in the diffraction pattern represent the LSMO, STO, and Pt respectively, with the coincidence of LSMO and STO diffraction spots (which appear yellow) being consistent with the epitaxial relationship and lack of strain relaxation across the cross-section. The pseudocubic structure of perovskites makes twinning relatively common and the (111) twinning plane observed here is similar to twinned structures seen in $BaTiO_3$[65] and $SrRuO_3$[66] systems. An electron diffraction study of the latter[66] highlighted a pattern including 1/6 fractional spots aligned at 70.7° to the bulk pattern, just as in Figure 2d. This microtwinning can be considered as a stacking fault in the close-packed (111) layers and to our knowledge has not been described in LSMO

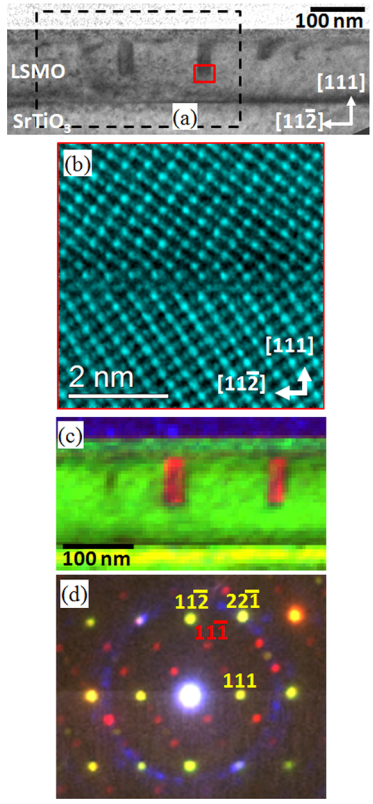

Figure 2. (a) Low-magnification bright field image of the LSMO cross-section, where the bottom of a crystal defect is highlighted by a red box. (b) High-angle annular dark field image of the twin boundary defect highlighted by the red box. (c) Scanning diffraction collected within the dashed black rectangle of (a) and colored in accordance with (d) color-coded selected area diffraction patterns. Rectangular red defects within the LSMO produced the red spots in the diffraction pattern; LSMO (green) is epitaxially aligned with the STO (yellow) and the polycrystalline Pt cap (blue) produces a diffraction ring.[51]

DOI: 10.1021/acs.nanolett.5b01953
Nano Lett. 2015, 15, 5868–5874

previously. Although we assume the twin defects observed here to be an artifact of the cross-section preparation rather than arising during growth, the results below suggest that inducing such defects may provide a means of controlling magnetic domain wall propagation.

Figure 3 shows a map of specimen thickness, which was acquired using the EELS spectrum imaging technique.[67] The

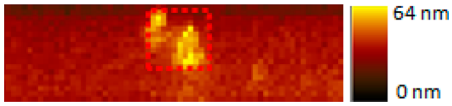

Figure 3. A thickness map of the LSMO cross-section nanowire, acquired in situ by EELS, shows good uniformity apart from a small region close to the defect (indicated by the red dashed box), where prolonged imaging resulted in a buildup of carbon under the electron beam.[51]

log-ratio method[68] was used to determine the relative thickness at each pixel, assuming negligible variation of material parameters throughout the film thickness. An electron mean free path[69] and thereby an absolute thickness was derived using the mean atomic number of LSMO. Note that the thicker region enclosed by the red square was an effect of prolonged scanning of the beam, resulting in an excess of carbon at this location, and can be ignored. The thickness increases by ~10.5 nm across a ~ 1 μm distance, thus creating a slight wedge with a mean thickness of 35 nm (excluding the region of carbon contamination). Using spectroscopy to determine the sample thickness in situ is important, because it enables the integrated magnetic induction, B_st, obtained from the DPC images to be converted to a value of B_s, as explored below.

Interestingly, in situ magnetizing experiments carried out at 100 K resulted in the trapping of a head-to-head magnetic DW by the crystal defect, as illustrated by the DPC image in Figure 4a. (The orthogonal components used to generate the DPC image are presented in the Supporting Information.) The DW structure observed here arises as a result of the shape anisotropy and two-dimensional behavior induced by the constrained "nanowire" geometry and is comparable to that typically found in soft ferromagnetic nanowires such as permalloy.[70] It is similar in appearance to an asymmetric transverse DW[71] and has a width of 85 nm, which is in agreement with the expectation of a linear scaling of the extent of the wall with the nanowire width.[72] Vortex DW structures have previously been observed in a similar TEM lamella, grown on a (100) oriented substrate and prepared in cross-section to have similar dimensions and shape anisotropy to those here.[73] We confirmed the vortex state to be the lowest energy configuration using OOMMF[74] micromagnetic simulations (see Supporting Information for details). We therefore assume that pinning of the DW by the defect stabilizes the metastable structure and/or lowers the net DW energy. Indeed, the apex of the magnetic transverse wall (i.e., the intersection of the two wall sections constituting the transverse DW packet), aligns well with the structural twin boundary.

It may be observed that a 30 nm wide region at the top of the LSMO has a different appearance to the remainder of the nanowire and appears pink in Figure 4a but is believed to be magnetically dead, that is, that its magnetic induction is quenched. As discussed elsewhere,[75] contrast in DPC imaging can have nonmagnetic contributions, most notably electrostatic phase contributions (or changes in the thickness-integrated

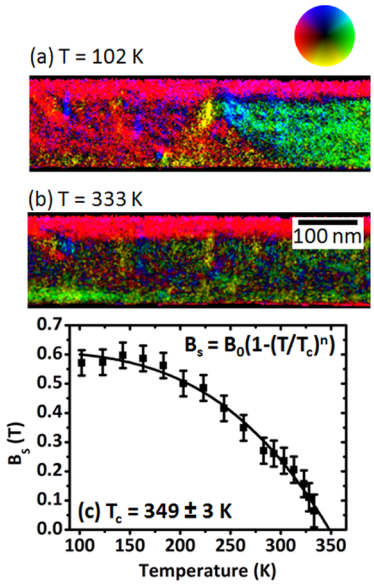

Figure 4. (a) DPC image of a head-to-head magnetic domain wall pinned at one of the crystal defects, collected at a temperature of 102 K. (b) DPC of the same region after heating to 333 K, where the magnetic signal is significantly reduced. Residual contrast is nonmagnetic in origin. (c) The saturation induction is plotted as a function of temperature and the Curie temperature was found to be 349 ± 3 K, averaged over the magnetic regions.[51]

inner potential) near the boundaries between materials of different atomic number or thickness. These nonmagnetic contributions can be distinguished from Lorentz phase contrast because they do not change as the LSMO approaches its Curie temperature, as illustrated by the DPC image in Figure 4b, which was collected at 333 K. While the rest of the LSMO loses DPC contrast, the pink region is retained at 333 K and so is not magnetic in origin. That same region appears as a slightly darker stripe in STEM image of Figure 2a but is colored green in Figure 2c, indicating that it is defective but retains its crystalline character, coherent with the rest of the film. The basic perovskite periodicity is retained. The region extends too far to be consistent with the magnetic dead layer discussed elsewhere[29,30] but previous work (e.g., ref 76.) has indicated that chemical reduction of LSMO, and the loss of oxygen from the lattice, can depress the Curie temperature of LSMO without changing its apparent crystallinity, which we assume also occurs here. What is surprising is the abrupt nature of the transition between the magnetic and nonmagnetic regions of the film, as one might otherwise expect a defect gradient that would give rise to a gradient in the magnitude of the magnetic induction.

A sensitive measure of the impact of defects is to determine the Curie temperature, which we achieve here with 3.5 nm spatial resolution using DPC Lorentz microscopy. The average saturation induction, B_S, was found to be 0.61 ± 0.02 T (using the 102 K data of Figure 3a and a mean sample thickness of 35 nm), slightly smaller than the 0.65 T of the original as-deposited film (see Supporting Information), which is expected to be the result of a small amount of surface damage caused by the ion milling process. Alongside the 102 K data, images were then acquired at regular intervals up to 333 K, ending with the DPC image in Figure 4b. The average saturation induction as a function of temperature is plotted in Figure 4c. By fitting a function of the form $B_S(1 - T/T_c)^n$ to the data, the Curie

DOI: 10.1021/acs.nanolett.5b01953
Nano Lett. 2015, 15, 5868−5874

temperature, T_c, was found to be 349 ± 3 K. The value of n = 17 was determined by fitting the whole data set, which is in good agreement with values found elsewhere[77−80] and with the as-grown value of 353 K. The retention of a high T_c is important here because it indicates that the FIB preparation has had minimal detrimental effect on the specimen because Ga^+ implantation has been shown to decrease T_c.[81]

Using the Curie temperature, the exchange stiffness can also now be estimated using molecular field theory.[82] Assuming the magnetic interaction is limited to the Mn sites with coordination number Z = 6, a spin S = 3/2, and lattice parameter a = 3.9 Å, molecular field theory yields $J \approx 3K_BT_c/2ZS(S+1) = 3.23 \times 10^{-22}$ J. The volume exchange stiffness, A, is related to the quantum mechanical exchange stiffness, J, in a cubic system by the relation $A = JS^2/a$, where S is the spin of the local moments and a is the lattice parameter. This produces an exchange stiffness constant, A_{ex}, of 1.86 pJ/m, which is in good agreement with the literature, which suggests values between 1.7[59] and 1.5 pJ/m.[83] Measuring the exchange stiffness is not trivial and is typically done through the excitation of spin waves by light,[84] neutrons,[85] or microwaves.[86] Although the method presented here does not provide a direct measure of A_{ex}, this is an important result, as it demonstrates the feasibility of measuring fundamental material properties using electron microscopy alone.

The values of B_s and T_c were extracted by integrating the image intensity over a number of pixels in order to reduce noise, however, these properties may also be mapped locally in order to assess the influence of defects. Maps of B_s and T_c are given in Figure 5a,b and were determined using both the DPC data and the EELS thickness map. Here, a plot of magnetic induction as a function of temperature was generated on a pixel-wise basis and fitted to the same function as used above; while inherently noisy, the maps provide a clear visual indication of the spatial trends across the image. The map of B_s in Figure 5a is predominantly green in the LSMO with blue/orange fluctuations. (Note that the pink band in Figure 5a corresponds to the magnetically dead region; the function could not be fitted to this region and as a result the B_s value is zero.) A slight reduction in B_s can be observed in both the rectangular defect and the triangular region within the DW (orange region) with a local mean B_s of 0.4 T. A reduction at the defect can be attributed to the change in bonding configuration across the twinning boundary, which will affect the double exchange mechanism underlying the ferromagnetism. The DPC measurement at the twin boundary itself is also susceptible to intensity fluctuations within the diffraction disk due to the change in crystallography[53] to which we attribute the blue right-angled lines to the right and bottom of the defect (see Supporting Information). Apparent reductions within the triangular region of the DW itself are more surprising because the wall is not a fixed structure. However, irrespective of where the DW is positioned, thermal fluctuations of the spins within the wall may be expected to be more facile than in regions of uniform magnetization and the time-averaged, in-plane B_s may therefore be reduced. The map of T_c appears predominantly green, indicating that there is little variation in the local T_c values, which cluster sharply around the mean value of 347 K, as evidenced by the histogram in Figure 5c (the magnetically dead region has been excluded from this plot.) A slight depression in T_c is also evident in the region of the DW, which correlates nicely to the fluctuations observed in the map of B_s. Some correlation between the maps of T_c and B_s is also clear throughout the rest of the LSMO, particularly at presumably defective regions along the upper edge of the wire. A comparison with the DPC image of the DW suggests that there are greater fluctuations near defects, which has implications for device applications and thus emphasizes the importance of atomic scale magnetic characterization in improving our understanding of defects in nanoscale systems.

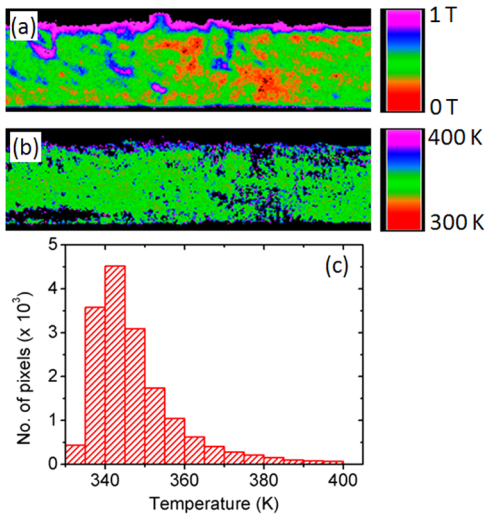

Figure 5. Pixel-wise maps of (a) the magnitude of the saturation induction and (b) the Curie temperature highlight local variations due to defects. (Note that the color-scale in a represents magnitude only, not direction, making small variations easier to discern.) Some fluctuations appear at the location of the twin defect and pinned DW. (c) A histogram of the T_c map with a peak around 345 K. The tail of the distribution above ~350 K is an artifact of pixel-by-pixel noise.[51]

SUMMARY AND CONCLUSIONS

Using electron microscopy techniques alone, the magnetic anisotropy of a free-standing LSMO(111) film has been determined and was found to be comparable to that of (110) orientated LSMO films. Consequently, unusually narrow DWs were observed compared with those typically found in the ferromagnetic manganites, which was attributed to mild strain in the film. These results illustrate a method of controlling magnetic anisotropy in LSMO thin films through strain engineering and provide new insights into mechanically induced anisotropy in LSMO(111). Additionally, well-defined twin boundary defects were observed to effectively pin magnetic DWs, suggesting that greater control over their formation may allow further control over the behavior of DWs in future devices.

A particularly important aspect of these results is the spatially resolved study linking defects in the physical structure of LSMO to its magnetic functionality, which is here presented with 3.5 nm spatial resolution. Throughout the length of the TEM lamella, we detected an abrupt transition from a magnetic region to a nonmagnetic layer near the surface of the film, even though the crystal structure was superficially intact, suggesting that surface damage can have a profound effect on the bulk performance of LSMO that may not be detectable by diffractive techniques alone. Our data also reveal details of the thermal behavior of spin structures inside a structurally pinned magnetic domain wall. We reveal nanoscale fluctuations in T_c and B_s in the vicinity of structural defects and aligned with the domain

DOI: 10.1021/acs.nanolett.5b01953
Nano Lett. 2015, 15, 5868−5874

wall edges, thus demonstrating the significance of defect characterization for potential device applications using these materials.

Finally, the techniques described here have allowed us to measure the local saturation induction, Curie temperature, anisotropy and exchange stiffness by Lorentz microscopy alone. We therefore emphasize that our method can determine magnetic parameters for a nanoscale region of material and can be used to characterize nanodevices, where such parameters are difficult to determine using conventional techniques.

■ ASSOCIATED CONTENT

Supporting Information

The Supporting Information is available free of charge on the ACS Publications website at DOI: 10.1021/acs.nanolett.5b01953.

Details of the differential phase contrast imaging technique, micromagnetic simulation, and characterization of the as-deposited LSMO film are included. (PDF)

■ AUTHOR INFORMATION

Corresponding Author

*E-mail: Donald.MacLaren@glasgow.ac.uk.

Notes

The authors declare no competing financial interest.

■ ACKNOWLEDGMENTS

This work was funded by EU's seventh framework Program IFOX (NMP3-LA-2010 246102) and the Engineering and Physical Sciences Research Council of the UK (EP/I00419X/1). The authors declare no competing financial interest.

■ REFERENCES

(1) Lu, H.; George, T. A.; Wang, Y.; Ketsman, I.; Burton, J. D.; Bark, C.-W.; Ryu, S.; Kim, D. J.; Wang, J.; Binek, C.; Dowben, P. A.; Sokolov, A.; Eom, C.-B.; Tsymbal, E. Y.; Gruverman, A. *Appl. Phys. Lett.* **2012**, *100*, 232904.

(2) Vaz, C. A. F. *J. Phys.: Condens. Matter* **2012**, *24*, 333201.

(3) Leufke, P. M.; Kruk, R.; Brand, R. A.; Hahn, H. *Phys. Rev. B: Condens. Matter Mater. Phys.* **2013**, *87*, 094416.

(4) Zhu, Q. X.; Zheng, M.; Yang, M. M.; Li, X. M.; Wang, Y.; Shi, X.; Chan, H. L. W.; Luo, H. S.; Li, X. G.; Zheng, R. K. *Appl. Phys. Lett.* **2013**, *103*, 132910.

(5) Binek, C.; Burobina, V. *Appl. Phys. Lett.* **2013**, *102*, 031915.

(6) Tokura, Y. *Rep. Prog. Phys.* **2006**, *69*, 797.

(7) Ramesh, R.; Spaldin, N. A. *Nat. Mater.* **2007**, *6*, 21.

(8) Perna, P.; Rodrigo, C.; Jiménez, E.; Teran, F. J.; Mikuszeit, N.; Méchin, L.; Camarero, J.; Miranda, R. *J. Appl. Phys.* **2011**, *110*, 013919.

(9) Schumacher, D.; Steffen, A.; Voigt, J.; Schubert, J.; Brückel, Th.; Ambaye, H.; Lauter, V. *Phys. Rev. B: Condens. Matter Mater. Phys.* **2013**, *88*, 144427.

(10) Dho, J.; Kim, Y. N.; Hwang, Y. S.; Kim, J. C.; Hur, N. H. *Appl. Phys. Lett.* **2003**, *82*, 1434.

(11) Suzuki, Y.; Wu, Y.; Yu, J.; Ruediger, U.; Kent, A. D.; Nath, T. K.; Eom, C. B. *J. Appl. Phys.* **2000**, *87*, 6746.

(12) Haghiri-Gosnet, A. M.; Wolfman, J.; Mercey, B.; Simon, Ch.; Lecoeur, P.; Korzenski, M.; Hervieu, M.; Desfeux, R.; Baldinozzi, G. *J. Appl. Phys.* **2000**, *88*, 4257.

(13) Stankevič, V.; Šimkevicius, Č.; Balevičius, S.; Žurauskienė, N.; Cimmperman, P.; Abrutis, A.; Plaušinaitienė, V. *Thin Solid Films* **2013**, *540*, 194.

(14) Demidov, V. V.; Ovsyannikov, G. A.; Petrzhik, A. M.; Borisenko, I. V.; Shadrin, A. V.; Gunnarsson, R. *J. Appl. Phys.* **2013**, *113*, 163909.

(15) Mathews, M.; Jansen, R.; Rijnders, G.; Lodder, J. C.; Blank, D. H. A. *Phys. Rev. B: Condens. Matter Mater. Phys.* **2009**, *80*, 064408.

(16) Nishikawa, H.; Houwman, E.; Boschker, H.; Mathews, M.; Blank, D. H. A.; Rijnders, G. *Appl. Phys. Lett.* **2009**, *94*, 042502.

(17) Suzuki, Y.; Hwang, H. Y.; Cheong, S.-W.; Van Dover, R. B. *Appl. Phys. Lett.* **1997**, *71*, 140.

(18) Berndt, L. M.; Balbarin, V.; Suzuki, Y. *Appl. Phys. Lett.* **2000**, *77*, 2903.

(19) Steenbeck, K.; Hiergeist, R. *Appl. Phys. Lett.* **1999**, *75*, 1778.

(20) Lecoeur, P.; Trouilloud, P. L.; Xiao, G.; Gupta, A.; Gong, G. Q.; Li, X. W. *J. Appl. Phys.* **1997**, *82*, 3934.

(21) Houwman, E. P.; Maris, G.; De Luca, G. M.; Niermann, N.; Rijnders, G.; Blank, D. H. A.; Speller, S. *Phys. Rev. B: Condens. Matter Mater. Phys.* **2008**, *77*, 184412.

(22) Mathews, M.; Postma, F. M.; Lodder, J. C.; Jansen, R.; Rijnders, G.; Blank, D. H. A. *Appl. Phys. Lett.* **2005**, *87*, 242507.

(23) Kubota, M.; Taniuchi, T.; Yasuhara, R.; Kumigashira, H.; Oshima, M.; Ono, K.; Okazaki, H.; Wakita, T.; Yokoya, T.; Akinaga, H.; Lippmaa, M.; Kawasaki, M.; Koinuma, H. *Appl. Phys. Lett.* **2007**, *91*, 182503.

(24) Wang, Z.-H.; Cristiani, G.; Habermeier, H.-U. *Appl. Phys. Lett.* **2003**, *82*, 3731.

(25) Rhensius, J.; Vaz, C. A. F.; Bisig, A.; Schweiter, S.; Heidler, J.; Körner, H. S.; Locatelli, A.; Niño, M. A.; Weigand, M.; Méchin, L.; Gaucher, F.; Goering, E.; Heyderman, L. J.; Kläui, M. *Appl. Phys. Lett.* **2011**, *99*, 062508.

(26) Chuang, D. S.; Ballentine, C. A.; O'Handley, R. C. *Phys. Rev. B: Condens. Matter Mater. Phys.* **1994**, *49*, 15084.

(27) Majumdar, S.; Huhtinen, H.; Paturi, P.; Majumdar, H. S. *J. Mater. Sci.* **2013**, *48*, 2115.

(28) Wahler, M.; Büttner, B.; Blaschek, H.-H.; Homonnay, N.; Wid, O.; O'Shea, K. J.; McGrouther, D.; MacLaren, D. A.; Schmidt, G. *Appl. Phys. Lett.* **2014**, *104*, 052408.

(29) Tebano, A.; Aruta, C.; Sanna, S.; Medaglia, P. G.; Balestrino, G.; Sidorenko, A. A.; De Renzi, R.; Ghiringhelli, G.; Braicovich, L. *Phys. Rev. Lett.* **2008**, *100*, 137401.

(30) Pesquera, D.; Wojcik, M.; Jedryka, E.; Laukhin, V.; Dix, N.; Sánchez, F.; Herranz, G.; Fontcuberta, J. *Adv. Mater. Interfaces* **2014**, *1*, 1400079.

(31) Chakhalian, J.; Millis, A. J.; Rondinelli, J. *Nat. Mater.* **2012**, *11*, 92.

(32) Gibert, M.; Zubko, P.; Scherwitzl, R.; Íñiguez, J.; Triscone, J.-M. *Nat. Mater.* **2012**, *11*, 195.

(33) Lecoeur, P.; Trouilloud, P. L.; Xiao, G.; Gupta, A.; Gong, G. Q.; Li, X. W. *J. Appl. Phys.* **1997**, *82*, 3934.

(34) Bakaul, S.; Lin, W.; Wu, T. *Appl. Phys. Lett.* **2011**, *99*, 042503.

(35) Olson, T. W.; Olsen, J. M. W.; Scholl, A.; Suzuki, Y. *J. Appl. Phys.* **2004**, *95*, 7354.

(36) Takamura, Y.; Chopdekar, R. V.; Scholl, A.; Doran, A.; Liddle, J. A.; Harteneck, B.; Suzuki, Y. *Nano Lett.* **2006**, *6*, 1287.

(37) Reeve, R. M.; Mix, C.; König, M.; Foerster, M.; Jakob, G.; Kläui, M. *Appl. Phys. Lett.* **2013**, *102*, 122407.

(38) Kim, E. J.; Watts, J. L. R.; Harteneck, B.; Scholl, A.; Young, A.; Doran, A.; Suzuki, Y. *J. Appl. Phys.* **2011**, *109*, 07D712.

(39) Zabaleta, J.; Valencia, S.; Kronast, F.; Moreno, C.; Abellán, P.; Gázquez, J.; Sepehri-Amin, H.; Sandiumenge, F.; Puig, T.; Mestres, N.; Obradors, X. *Nanoscale* **2013**, *5*, 2990.

(40) Heidler, J.; Rhensius, J.; Vaz, C. A. F.; Wohlhüter, P.; Körner, H S.; Bisig, A.; Schweitzer, S.; Farhan, A.; Méchin, L.; Le Guyader, L.; Nolting, F.; Locatelli, A.; Mentes, T. O.; Nino, M. A.; Kronast, F.; Heyderman, L. J.; Kläui, M. *J. Appl. Phys.* **2012**, *112*, 103921.

(41) Scheinfein, M. R.; Unguris, J.; Kelley, M. H.; Pierce, D. T.; Celotta, R. J. *Rev. Sci. Instrum.* **1990**, *61*, 2501.

(42) Petford-Long, A. K.; Chapman, J. N. Lorentz Microscopy. In *Magnetic Microscopy of Nanostructures*; Hopster, H., Oepen, H. P., Eds.; Springer: Berlin, 2005; pp 67−86.

(43) Phatak, C.; Liu, Y.; Gulsoy, E. B.; Schmidt, D.; Franke-Schubert, E.; Petford-Long, A. *Nano Lett.* **2014**, *14*, 759.

DOI: 10.1021/acs.nanolett.5b01953
Nano Lett. 2015, 15, 5868−5874

(44) Van Tendeloo, G.; Bals, S.; Van Aert, S.; Verbeeck, J.; Van Dyck, D. *Adv. Mater.* **2012**, *24*, 5655.
(45) Colliex, C. J. *Microscopy* **2011**, *60*, S161.
(46) McVitie, S.; McGrouther, D.; McFadzean, S.; MacLaren, D. A.; O'Shea, K. J.; Benitez, M. J. *Ultramicroscopy* **2015**, *152*, 57.
(47) Moshnyaga, V.; Khoroshun, I.; Sidorenko, A.; Petrenko, P.; Weidinger, A.; Zeitler, M.; Rauschenbach, B.; Tidecks, R.; Samwer, K. *Appl. Phys. Lett.* **1999**, *74*, 2842.
(48) O'Shea, K. J.; McGrouther, D.; Ferguson, C.; Jungbauer, M.; Hühn, S.; Moshnyaga, V.; MacLaren, D. A. *Micron* **2014**, *66*, 9.
(49) Langford, R. M.; Petford-Long, A. K. *J. Vac. Sci. Technol., A* **2001**, *19*, 2186.
(50) Chapman, J. N.; McFadyen, I. R.; McVitie, S. *IEEE Trans. Magn.* **1990**, *26*, 1506.
(51) The data used to compile this figure is available at http://dx.doi.org/10.5525/gla.researchdata.203; University of Glasgow Data Registry (accessed Dec 8, 2015).
(52) Williams, D. B.; Carter, C. B. *Transmission Electron Microscopy*; Springer: New York, 1996; pp 369−378.
(53) MacLaren, I.; Wang, L. Q.; McGrouther, D.; Craven, A. J.; McVitie, S.; Schierholz, R.; Kovács, A.; Barthel, J.; Dunin-Borkowski, R. E. *Ultramicroscopy* **2015**, *154*, 57.
(54) McVitie, S.; Cushley, M. *Ultramicroscopy* **2006**, *106*, 423.
(55) Lloyd, S. J.; Mathur, N. D.; Louden, J. C.; Midgely, P. A. *Phys. Rev. B: Condens. Matter Mater. Phys.* **2001**, *64*, 172407.
(56) Murakami, Y.; Kasai, H.; Kim, J. J.; Mamishin, S.; Shindo, D.; Mori, S.; Tonomura, A. *Nat. Nanotechnol.* **2010**, *5*, 37.
(57) Jiles, D. *Introduction to Magnetism and Magnetic Materials*; Chapman & Hall: New York, 1998; pp 161−162.
(58) Nagai, T.; Yamada, H.; Konoto, M.; Arima, T.; Kawasaki, M.; Kimoto, K.; Matsui, Y.; Tokura, Y. *Phys. Rev. B: Condens. Matter Mater. Phys.* **2008**, *78*, 180414.
(59) Wang, Z.; Li, Y.; Viswan, R.; Hu, B.; Harris, V. G.; Li, J.; Viehland, D. *ACS Nano* **2013**, *7*, 3447.
(60) Zhai, Z. Y.; Wu, X. S.; Jiang, Z. S.; Hao, J. H.; Gao, J.; Cai, Y. F.; Pan, Y. G. *Appl. Phys. Lett.* **2006**, *89*, 262902.
(61) Peng, L. S.-J.; Xi, X. X.; Moeckly, B. H.; Alpay, S. P. *Appl. Phys. Lett.* **2003**, *83*, 4592.
(62) Huang, Q. J.; Cheng, Y.; Liu, X. J.; Xu, X. D.; Zhang, S. Y. *Ultrasonics* **2006**, *44*, 223.
(63) Liu, C.-C.; Chu, P.-Y.; Chiang, Y. W.; Juang, J.-H.; Jen, S.-U. *J. Phys. D: Appl. Phys.* **2013**, *46*, 255001.
(64) Hayashi, M.; Thomas, L.; Rettner, C.; Moriya, R.; Jiang, X.; Parkin, S. S. P. *Phys. Rev. Lett.* **2006**, *97*, 207205.
(65) Rećnik, A.; Bruley, J.; Mader, W.; Kolar, D.; Rühle, M. *Philos. Mag. B* **1994**, *70*, 1021.
(66) Han, Y.; Reaney, I. M.; Tinberg, D. S.; Trolier-McKinstry, S. *Acta Crystallogr., Sect. B: Struct. Sci.* **2009**, *65*, 694.
(67) Jeanguillaume, C.; Colliex, C. *Ultramicroscopy* **1989**, *28*, 252.
(68) Egerton, R. F. *Electron Energy-Loss Spectroscopy in the Electron Microscope*, 3rd ed.; Springer: New York, 2011.
(69) Malis, T.; Cheng, S. C.; Egerton, R. F. *J. Electron Microsc. Tech.* **1988**, *8*, 193.
(70) Sandweg, C. W.; Wiese, N.; McGrouther, D.; Hermsdoerfer, S. J.; Schultheiss, H.; Leven, B.; McVitie, S.; Hillebrands, B.; Chapman, J. N. *J. Appl. Phys.* **2008**, *103*, 093906.
(71) Nakatani, Y.; Thiaville, A.; Miltat, J. *J. Magn. Magn. Mater.* **2005**, *290*, 750.
(72) Klaui, M. *J. Phys.: Condens. Matter* **2008**, *20*, 313001.
(73) Nagai, T.; Yamada, H.; Konoto, M.; Arima, T.; Kawasaki, M.; Kimoto, K.; Matsui, Y.; Tokura, Y. *Phys. Rev. B: Condens. Matter Mater. Phys.* **2008**, *78*, 180414.
(74) http://math.nist.gov/oommf/software-12.html; National Institute of Standards and Technology (accessed Jan 20, 2015).
(75) Chapman, J. N. *Mater. Sci. Eng., B* **1989**, *3*, 355.
(76) Brivio, S.; Magen, C.; Sidorenko, A.; Petti, D.; Cantoni, M.; Finazzi, M.; Ciccacci, F.; De Renzi, R.; Varela, M.; Picozzi, S.; Bertacco, R. *Phys. Rev. B: Condens. Matter Mater. Phys.* **2010**, *81*, 094410.
(77) Weber, M. C.; Hillebrands, B.; Moshnyaga, V.; Samwer, K. *Europhys. Lett.* **2006**, *73*, 285.
(78) Haghiri-Gosnet, A.-M.; Renard, J.-P. *J. Phys. D: Appl. Phys.* **2003**, *36*, R127.
(79) Zabaleta, J.; Jaafar, M.; Abellán, P.; Montón, C.; Iglesias-Freire, O.; Sandiumenge, F.; Ramos, C. A.; Zysler, R. D.; Puig, T.; Asenjo, A.; Mestres, N.; Obradors, X. *J. Appl. Phys.* **2012**, *111*, 024307.
(80) Fadil, D.; Wu, S.; Perna, P.; Renault, B.; Saïb, M.; Lebargy, S.; Gasnier, J.; Guillet, B.; Routoure, J.-M.; Flament, S.; Méchin, L. *J. Appl. Phys.* **2012**, *112*, 013906.
(81) Hao, C.; Zhao, B.; Kuang, G.; Sun, Y. *Phys. Status Solidi B* **2011**, *248*, 2921.
(82) Coey, J. M. D. *Magnetism and Magnetic Materials*; Cambridge University Press: New York, 2010.
(83) Wohlhüter, P.; Rhensius, J.; Vaz, C. A. F.; Heidler, J.; Körner, H. S.; Bisig, A.; Foerster, M.; Méchin, L.; Gaucher, F.; Locatelli, A.; Niño, M. A.; El Moussaoui, S.; Nolting, F.; Goering, E.; Heyderman, L. J.; Kläui, M. *J. Phys.: Condens. Matter* **2013**, *25*, 176004.
(84) Liu, X.; Steiner, M. M.; Sooryakumar, R.; Prinz, G. A.; Farrow, R. F. C.; Harp, G. *Phys. Rev. B: Condens. Matter Mater. Phys.* **1996**, *53*, 12166.
(85) Hüller, K. *J. Magn. Magn. Mater.* **1986**, *61*, 347.
(86) Farle, M. *Rep. Prog. Phys.* **1998**, *61*, 755.

DOI: 10.1021/acs.nanolett.5b01953
Nano Lett. 2015, 15, 5868−5874